

# Vision-Based PM<sub>2.5</sub> Concentration Estimation With Natural Scene Statistical Analysis

Guangcheng Wang, Quan Shi, *Member, IEEE*, Han Wang, Ke Gu, *Senior Member, IEEE*,  
Mengting Wei, Lai Kuan Wong, *Member, IEEE*, and Mingxing Wang

**Abstract**—As the primary pollutant in China's urban atmosphere, PM<sub>2.5</sub> poses a great threat to the health of residents and ecological stability. Efficient and effective PM<sub>2.5</sub> concentration monitoring is essential. Nonetheless, the popular devices for PM<sub>2.5</sub> monitoring are developed based on two standards: the micro-oscillation balance method and the  $\beta$ -ray method, which have high purchase and maintenance costs and slow calculation rates. To this end, we put forward a real-time and reliable vision-based estimation algorithm of PM<sub>2.5</sub> concentration. To be specific, the proposed method first develops two natural scene statistical analysis-based visual priors to measure saturation and structural information losses caused by the 'haze' formed by PM<sub>2.5</sub>. Moreover, we develop a lightweight deep belief network (DBN)-deep neural network (DNN)-based PM<sub>2.5</sub> concentration estimation model, which learns the mapping from the designed visual priors to PM<sub>2.5</sub> concentrations. Experiments confirm the superiority of our vision-based PM<sub>2.5</sub> concentration estimation method by comparison with state-of-the-art photo-based PM<sub>2.5</sub> monitoring methods.

**Impact Statement**—With the rapid development of computer vision technology, researchers try to design image processing algorithms to quickly estimate PM<sub>2.5</sub> concentration with the help of visual information. The vision-based PM<sub>2.5</sub> concentration estimation algorithm can effectively overcome the shortcomings of traditional PM<sub>2.5</sub> concentration measurement methods such as long time consumption and high maintenance cost. However, existing studies show that the performance of the current picture-based PM<sub>2.5</sub> concentration measurement algorithms is limited by the diversity of image scene content. The proposed PM<sub>2.5</sub> concentration estimation algorithm based on natural scene statistical analysis overcomes this limitation. On the public air quality image database, the accuracy of the proposed method reaches 88%, which exceeds the performance of the mainstream methods. Our method is easy to implant some edge smart devices, such as smartphones, monitoring devices, and dash cams.

**Index Terms**—PM<sub>2.5</sub> concentration estimation, natural scene statistical analysis, vision, saturation, structure.

This work was supported in part by the Beijing Natural Science Foundation under Grant JQ21014; in part by the National Science Foundation of China under Grant 62322302, Grant 62273011, Grant 62076013, Grant 42001239. (Corresponding authors: Ke Gu; Quan Shi.)

Guangcheng Wang, Quan Shi and Han Wang are with the School of Transportation and Civil Engineering, Nantong University, Nantong 226019, China (e-mail: wangguangcheng0428@163.com; sq@ntu.edu.cn; hanwang@ntu.edu.cn).

Ke Gu is with the Faculty of Information Technology, Engineering Research Center of Intelligence Perception and Autonomous Control, Ministry of Education, Beijing Laboratory of Smart Environmental Protection, Beijing Artificial Intelligence Institute, Beijing University of Technology, Beijing 100124, China (e-mail: guke.doctor@gmail.com).

Mengting Wei is with the Institute of Software, Chinese Academy of Sciences, Beijing, China (e-mail: verna\_wei@163.com).

Lai Kuan Wong is with the Faculty of Computing and Informatics, Multimedia University, Cyberjaya 63100, Malaysia (e-mail: lk Wong@mmu.edu.my).

Mingxing Wang is with the Century Rotek (Beijing) Environmental Science & Technology Co., Ltd., Beijing, China (e-mail: 1287005782@qq.com).

## I. INTRODUCTION

With the rapid development of urbanization and industrialization, the world is facing serious pollution problems, among which air pollution has become one of the key factors restricting urban development and affecting human health. [1]–[4]. Particulate matter is an important source of air pollution, among which fine particulate matter (PM<sub>2.5</sub>) is conducive to staying and spreading in the atmosphere due to its small particle size and is rich in harmful substances, which has a more significant impact on the atmospheric environment and human health [5]. Medical researches have shown that PM<sub>2.5</sub> in the near-surface air may be inhaled into the human lungs, resulting in serious health problems in the human respiratory, cardiovascular, reproductive, or blood systems [6]–[9].

PM<sub>2.5</sub> is rich in various organic compounds, among which polycyclic aromatic hydrocarbons are carcinogens, with strong toxicity, among which benzopyrene is the most carcinogenic [10]. In October 2013, the International Agency for Research on Cancer listed outdoor air pollution as one of the human carcinogens [11]. The Air Quality Guidelines issued by the World Health Organization in 2005 indicate that when the average annual concentration of PM<sub>2.5</sub> reaches 35 $\mu\text{g}/\text{m}^3$ , the human death risk is about 15% higher than that of 10 $\mu\text{g}/\text{m}^3$  [12]. Recently, several studies have shown that novel coronavirus disease 2019 (COVID-19) can propagate by aerosols, which indicates that PM<sub>2.5</sub>, as a type of aerosol, can also act as a carrier to facilitate the global spread of COVID-19, thus threatening to health and safety of humans [13]–[15].

PM<sub>2.5</sub> pollution seriously endangers human health and significantly impacts climate and atmospheric visibility. The aerosol particulate matter remains one of the most considerable uncertainties affecting global climate change [16]. The increased aerosol particles in the atmosphere can lead to a large-scale reduction in precipitation in polluted areas [17]. Bolasina *et al.* found that the changes in the concentration of anthropogenic aerosol particles may be the primary factor leading to the decrease in precipitation in South Asia in the mid-twentieth century [18]. The scattering and absorption of light by particulate matter in the atmosphere can significantly diminish the light signal and thus reduce substantially effective seeing distance. As a result, PM<sub>2.5</sub> can lead to reduced visibility in cities and 'haze' weather. Moreover, Sweerts *et al.* found that aerosols' scattering and absorption by solar radiation also strongly reduced the solar photovoltaic power production in China [19]. Therefore, effectively monitoring and controlling PM<sub>2.5</sub> concentration positively improves human health and the



Fig. 1: Examples of  $PM_{2.5}$  concentration monitoring equipment.

atmospheric environment.

To effectively monitor  $PM_{2.5}$  concentrations, many high-precision electronic instruments have been used in daily life as shown in Fig. 1, which are basically designed based on the gravimetric method,  $\beta$ -ray absorption method, and tapered element oscillating microbalance method [20]. The best-performing method among the three methods is the gravimetric method, which has long been regarded as the national standard analysis method [21]. The success of the  $\beta$ -ray absorption method lies in the principle of  $\beta$ -ray attenuation, which measures  $PM_{2.5}$  concentrations via computing the attenuation amount of  $\beta$ -ray energy. However, the accuracy of the  $\beta$ -ray absorption method depends on constant temperature and humidity. The tapered element oscillating microbalance method is developed based on the principle of micro-oscillating balance with conical elements of aerospace technology. The  $PM_{2.5}$  concentration at the corresponding time can be measured by estimating the change in the system frequency, and the measurement results are usually accurate. However, the  $PM_{2.5}$  monitoring equipment based on the tapered element oscillating microbalance method is large and expensive. The high-precision electronic instruments based on all three of the above methods have some drawbacks to limit their applicability to real-time  $PM_{2.5}$  monitoring with the high-density spatial distribution such as excellent working environments, a large size, high costs, and long sampling periods. Therefore, designing a more convenient  $PM_{2.5}$  concentration monitoring method has more theoretical research significance and practical application value. To this aim, we present a real-time and reliable vision-based  $PM_{2.5}$  concentration measurer. We highlight our main contributions below.

1) We develop two groups of natural scene statistical analysis (NSSA)-based visual priors for measuring the saturation and structure losses during the imaging process due to the ‘haze’ introduced by  $PM_{2.5}$ . The NSSA-based saturation loss visual prior combines the mean subtracted contrast normalized (MSCN) coefficients with the asymmetric generalized Gaussian distribution (AGGD) function to extract statistical features in the saturation domain. The NSSA-based structure loss visual prior segments sky regions of images based on the dark channel prior [22], and then estimates the  $PM_{2.5}$  concentration through computing the information entropy of the non-sky regions.

2) We present a lightweight deep belief network (DBN)-

deep neural network (DNN)-based  $PM_{2.5}$  concentration measurer, which learns the mapping of the designed NSSA-based visual priors to  $PM_{2.5}$  concentrations. The proposed lightweight DBN-DNN (LW-DBN-DNN) combines pruning with quantization for model compression, which makes our  $PM_{2.5}$  monitoring method easier to deploy on edge devices.

3) Experiments constructed on the public air quality image database (AQID) [23] demonstrate the advantages of our vision-based algorithm over the relevant state-of-the-art (SOTA)  $PM_{2.5}$  concentration measurement algorithms.

## II. RELATED WORKS

### A. Photo-Based $PM_{2.5}$ Concentration Estimation

Nowadays, high-quality images are easily available with image capture devices (e.g., smartphones, dash cams, and surveillance devices), and these edge devices can run image processing algorithms. Therefore, some researchers have tried to measure  $PM_{2.5}$  concentration by image information. For example, Gu *et al.* measured  $PM_{2.5}$  concentration based on the significant difference between the entropy features of high and low concentration  $PM_{2.5}$  images in the spatial and saturation transformation domains [23]. Wang *et al.* proposed a  $PM_{2.5}$  concentration estimation method based on image color, texture structure, entropy, and transmission [24]. In literature [25], the visual saliency technology is adopted to construct a  $PM_{2.5}$  concentration measurer, which estimates  $PM_{2.5}$  concentrations by calculating the entropy of the non-significant regions in the saturation map. The above entropy features-based  $PM_{2.5}$  concentration monitoring models are vulnerable to the diversity of image contents. For example, an image with more smooth regions has a low entropy value, easily misclassified as a high  $PM_{2.5}$  image. To alleviate the limitations of the above methods, Yue *et al.* calculated the loss of structural information by calculating the gradient similarity between image saturation and gray-scale maps and estimated the loss of color information by calculating the Weibull distribution of saturation maps [26]. Finally, the two losses were combined to estimate  $PM_{2.5}$  concentrations. Since the gray-scale information corresponding to  $PM_{2.5}$  images is also lost, Yue *et al.*’s method has a very limited ability to represent the image structure loss by relying on the gradient similarity between the saturation and gray-scale channels of  $PM_{2.5}$  images. Moreover, Yue *et al.*’s study showed that the distribution of the saturation map corresponding to the  $PM_{2.5}$  image is only roughly in line with Weibull distribution, which made it difficult to estimate color information loss accurately. In literatures [27], [28], Sun *et al.* and Wang *et al.* introduced the concept of image defogging enhancement to measure the  $PM_{2.5}$  concentration, which computes the self-similarity of the color, depth, gradient, and entropy of  $PM_{2.5}$  images and their corresponding defogging enhancement results to estimate  $PM_{2.5}$  concentrations. These two algorithms employ clean images enhanced by the defogging algorithms to weaken the effect of image content diversity on  $PM_{2.5}$  concentration estimation models. However, the development of the defogging algorithm is not perfect enough to limit the performance of the above methods. To address the shortcomings of the above-mentioned photo-based  $PM_{2.5}$  concentration

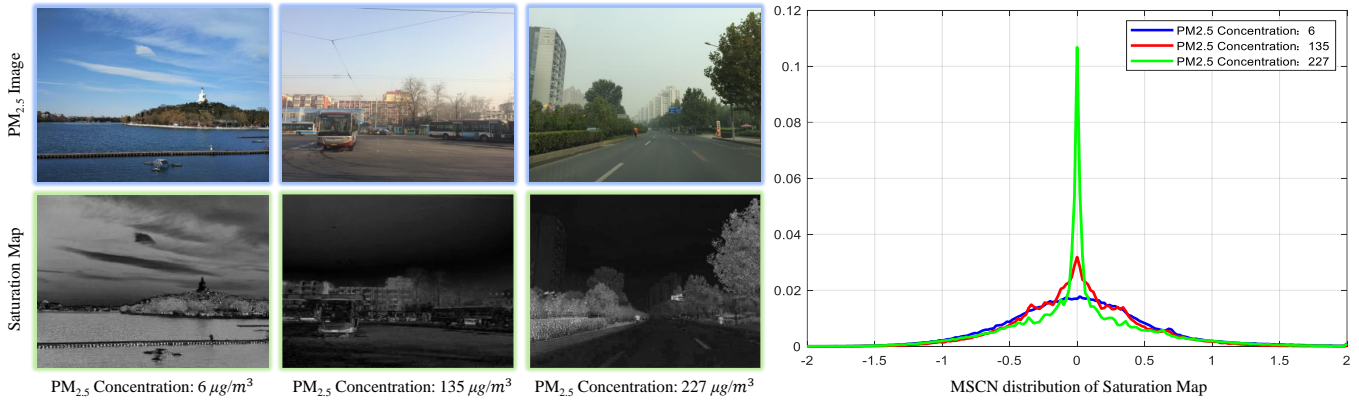


Fig. 2: The MSCN distributions of three  $PM_{2.5}$  pictures in the saturation domain.

estimation algorithms, we develop statistical features related to  $PM_{2.5}$  concentration from the angle of statistical analysis, which can largely effectively weaken the negative influence of visual content diversity on the robustness of  $PM_{2.5}$  monitoring models.

### B. Application of $PM_{2.5}$ Concentration Monitoring

The application significance of  $PM_{2.5}$  concentration monitoring system in environmental monitoring is not only to monitor numerical values, but also to establish a unified monitoring, evaluation, and coordination mechanism through standard monitoring methods [29], which has achieved the goals of reducing air pollutant emissions, improving air quality, enhancing regional environmental prevention and control.  $PM_{2.5}$  concentration monitoring is a key step in scientific prevention and control of air quality, which promotes the construction and development of smart cities in China [30].  $PM_{2.5}$  concentration monitoring is essential to residents' health, travel arrangements, and national environmental governance [31]–[34]. By estimating the concentrations of  $PM_{2.5}$ , air quality can be monitored promptly, providing a basis for urban management and environmental protection.  $PM_{2.5}$  concentration monitoring can help people manage their health well, thus avoiding outdoor activities in highly polluted environments and reducing health risks. For example, Gu *et al.* proposed a multi-task temporal support vector regression model to help decision-makers manage air quality at mass gatherings [35]. On the basis of accurately predicting air pollutants and comparing them with standard concentration indicators, managers can fully control ventilation systems and population distribution at mass gatherings to ensure public health. Industrial emissions (such as vehicle exhaust) are also important  $PM_{2.5}$  sources. Monitoring  $PM_{2.5}$  concentration can adjust pollutant discharge adaptively and realize automatic adjustment of traffic flow, thereby achieving the safety and smoothness of urban traffic. Wang *et al.* found that the low emissions of the transport sector and the secondary industry during the control period of COVID-19 were the main reasons for the decline of  $PM_{2.5}$ ,  $NO_2$  and CO concentrations [34].  $PM_{2.5}$  concentration is influenced by meteorological conditions, so estimating  $PM_{2.5}$  concentration can improve the accuracy of meteorological

forecasting and provide better services for people's production and life [1].

## III. PROPOSED VISION-BASED $PM_{2.5}$ CONCENTRATION ESTIMATION ALGORITHM

We will detail the developed vision-based  $PM_{2.5}$  concentration estimation algorithm from designing two types of NSSA-based visual priors and the LW-DBN-DNN-based  $PM_{2.5}$  concentration estimation model. We observe that the low- and high- $PM_{2.5}$  concentration images differ more significantly in saturation and dark channel domains. Therefore, we specifically develop two types of NSSA-based visual priors to quantify the saturation and structure losses owing to  $PM_{2.5}$ .

### A. The NSSA-based Visual Prior for The Saturation Loss

The studies have shown that the MSCN coefficients extracted from low-quality images due to artifacts such as blocking, blurring, and noise have statistically distributed properties in the spatial domain compared to high-quality images [36]–[38]. This is because there is a significant difference in the degradation of the images caused by this blocking, blur, and noise artifacts in the spatial domain. From Fig. 2, there is a clear difference between the saturation maps of the high- and low- $PM_{2.5}$  concentration images. Specifically, the pixel values of the high- $PM_{2.5}$  saturation maps are closer to zero than low- $PM_{2.5}$  saturation maps. Thus, we consider  $PM_{2.5}$  as a distortion that decreases the image quality and quantify the distortion intensity in the saturation transformation domain, i.e., measuring  $PM_{2.5}$  concentration. We analyze the distribution properties of MSCN coefficients on massive pictures with different  $PM_{2.5}$  concentrations. Fig. 2 shows the MSCN distributions of three images with  $PM_{2.5}$  concentrations of  $7 \mu g/m^3$ ,  $135 \mu g/m^3$  and  $227 \mu g/m^3$  in the saturation domain. From Fig. 2, we can observe that the MSCN coefficient histogram of different  $PM_{2.5}$  pictures in the saturation domain presents an asymmetric generalized Gaussian distribution. Therefore, the AGGD function is employed to fit the distribution shape and peak. The obtained fitting parameters are used as the first type of NSSA-based visual prior to estimating the saturation loss. Next, we describe the extraction process of the first type of NSSA-based visual prior in detail. First, we use Equation



(1) to convert  $PM_{2.5}$  images from RGB color space to HSV color space to obtain saturation information.

$$S = \begin{cases} \frac{\max(R,G,B) - \min(R,G,B)}{\max(R,G,B)}, & \text{if } \max(R,G,B) \neq 0 \\ 0, & \text{if } \max(R,G,B) = 0 \end{cases}, \quad (1)$$

where the  $\max(R,G,B)$  and  $\min(R,G,B)$  denote the maximum and minimum pixel values of the R, G, and B components of an RGB image, respectively.  $S$  is the obtained saturation map of a given  $PM_{2.5}$  image. Then, we subtract the mean and divide the variance of the pixel values of the saturation map  $S$  to obtain the MSCN coefficient. The specific calculation procedure is as follows.

$$MSCN_S(x,y) = \frac{S(x,y) - \mu(x,y)}{\sigma(x,y) + C}, \quad (2)$$

where the  $\mu(x,y) = \frac{\sum_{m=-M}^M \sum_{n=-N}^N \omega_{m,n} S_{m,n}(x,y)}{\sum_{m=-M}^M \sum_{n=-N}^N \omega_{m,n}}$  and  $\sigma(x,y) = \sqrt{\frac{\sum_{m=-M}^M \sum_{n=-N}^N \omega_{m,n} (S_{m,n}(x,y) - \mu(x,y))^2}{\sum_{m=-M}^M \sum_{n=-N}^N \omega_{m,n}}}$  are the calculation details of the mean and standard deviation, respectively, where  $\omega = \{\omega_{m,n} | k = -M, \dots, M, n = -N, \dots, N\}$  is the Gaussian weight function. The  $(x,y)$  is the pixel index. The parameters  $M$  and  $N$  are empirically set to 3 [36], [37].  $C$  is a small positive number to prevent the denominator from being zero. As mentioned above, the MSCN distribution of  $PM_{2.5}$  pictures in the saturation domain presents an asymmetric generalized gaussian distribution. So we employ the AGGD function to fit the MSCN distribution of  $PM_{2.5}$  pictures in the saturation domain. The AGGD function is defined below.

$$f(x; \alpha, \sigma_l^2, \sigma_r^2) = \begin{cases} \frac{\alpha}{(\beta_l + \beta_r) \Gamma(\frac{1}{\alpha})} \exp\left(-\left(\frac{-x}{\beta_r}\right)^\alpha\right), & x \geq 0, \\ \frac{\alpha}{(\beta_l + \beta_r) \Gamma(\frac{1}{\alpha})} \exp\left(-\left(\frac{-x}{\beta_l}\right)^\alpha\right), & x < 0, \end{cases} \quad (3)$$

where  $\Gamma(a) = \int_0^\infty t^{a-1} e^{-t} dt$  is gamma function.  $\beta_l = \sigma_l \sqrt{\frac{\Gamma(\frac{1}{\alpha})}{\Gamma(\frac{3}{\alpha})}}$  and  $\beta_r = \sigma_r \sqrt{\frac{\Gamma(\frac{1}{\alpha})}{\Gamma(\frac{3}{\alpha})}}$ .  $\sigma_l^2$  and  $\sigma_r^2$  are the left-scale and right-scale parameters, respectively, which control the diffusion degree of the left and right sides. The parameters  $\alpha$ ,  $\sigma_l^2$ , and  $\sigma_r^2$  are employed as the first type of NSSA-based visual prior to measuring the saturation loss.

### B. The NSSA-based Visual Prior for The Structure Loss

This part considers estimating the  $PM_{2.5}$  concentration directly from the perspective of quantifying the energy loss of image structure information. In the literature [39], He *et al.* proposed a dark channel prior, which is a statistic for fog-free outdoor images. The dark channel prior indicates that non-sky regions in a haze-free image have very low pixel values in at least one of the R, G, and B color channels. The dark channel of the haze image is visually brighter and can be seen as a rough approximation of the haze thickness. Based on He *et al.*'s findings, we plan to introduce the dark channel prior to estimating the structural information loss caused by  $PM_{2.5}$  during the imaging process. Fig. 3 illustrates some  $PM_{2.5}$  pictures with multi-level concentrations and their corresponding dark channels, from which we can easily learn

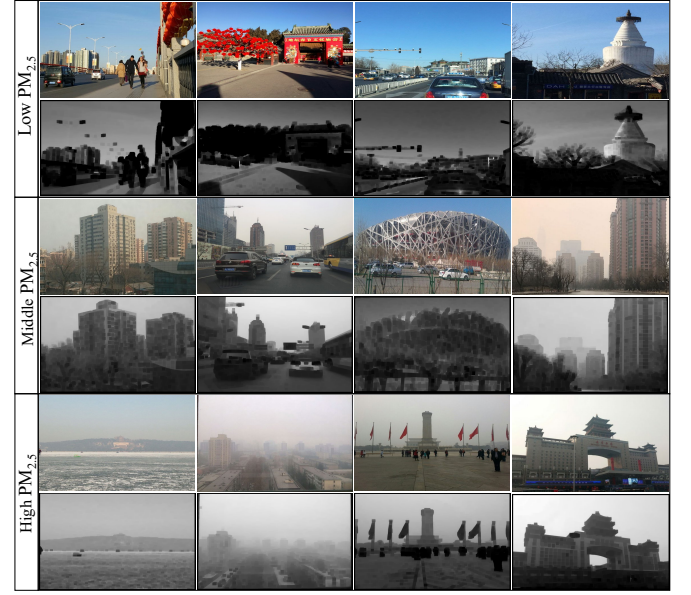


Fig. 3: Examples of different degrees of  $PM_{2.5}$  concentration images and their corresponding dark channels.

that the dark channels of the non-sky image blocks have noticeable visual differences under different  $PM_{2.5}$  concentrations, i.e., the higher  $PM_{2.5}$  concentration corresponds to higher luminance values in the dark channel. Inspired by this, we calculate the dark channel energy of non-sky image blocks to quantify the structural information loss caused by  $PM_{2.5}$ . Specifically, we first extract the dark channel information of images by adopting Equation (4).

$$I_{dark}(x,y) = \min_{(x,y) \in \Omega(x,y)} \left[ \min_{c \in \{R,G,B\}} I_c(x,y) \right], \quad (4)$$

where  $I_c$  represents the color channel of a given image  $I$ .  $\Omega(x,y)$  is a local block centered at  $(x,y)$ .  $\min_{(x,y) \in \Omega(x,y)}$  is a minimum filter. Next, we segment the non-sky and sky regions with the dark channel prior and further compute the dark channel energy mean of the non-sky image blocks as the quantitative result of the structure loss. The specific calculation details are as follows:

$$E_d = \frac{\sum T(I_{dark})(x,y) \cdot I_{dark}(x,y)^2}{\sum T(I_{dark})(x,y)}, \quad (5)$$

where  $T(\cdot)$  is a gray-thresh function [40] to binarize the dark channel image  $I_{dark}$ . The obtained  $E_d$  is the second type of NSSA-based visual prior developed for the structure loss.

### C. LW-DBN-DNN-based $PM_{2.5}$ Concentration Estimation Model

In existing studies on the photo-based  $PM_{2.5}$  concentration measurement, the support vector machine (SVM) is often used to fuse extracted image-aware features to estimate  $PM_{2.5}$  concentration [28], [41]. However, because of the shallow architecture of the SVM [42], it does not optimally map the perceptual features to  $PM_{2.5}$  concentration values. To overcome this problem, Sun *et al.* proposed to use DNN

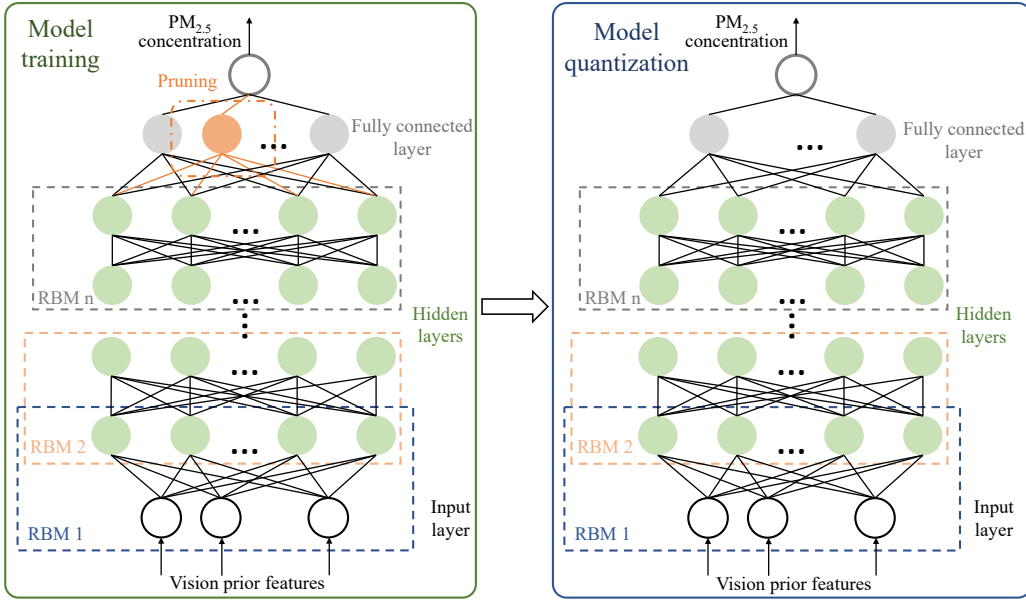


Fig. 4: Framework of the proposed LW-DBN-DNN-based  $PM_{2.5}$  concentration estimator.

to map features to  $PM_{2.5}$  concentration values [27]. Unfortunately, with a small training data size, DNN is prone to fall into local optimum and long training time due to random initialization of weight parameters. The training strategy of Hinton *et al.*'s DBN-DNN combining greedy unsupervised learning with supervised learning fine-tuning can effectively compensate for the deficiency of DNN on the small-scale database [43], [44]. Moreover, considering the application of the proposed  $PM_{2.5}$  monitor on edge devices, we combine pruning and quantization to carry out lightweight treatment of DBN-DNN. The obtained LW-DBN-DNN is used to learn the mapping of the proposed NSSA-based visual priors to  $PM_{2.5}$  concentrations. Fig. 4 illustrates the framework of the proposed LW-DBN-DNN-based  $PM_{2.5}$  concentration estimation model, which includes a DBN composed of multi-layer restricted Boltzmann machines (RBMs) (i.e., hidden layers) and a fully connected layer. We first adopt unsupervised greedy learning to update the parameters of DBN, that is, to initialize the parameters of the network's hidden layers. The specific parameter optimization method is shown in the literature [45]. After unsupervised pre-training, our  $PM_{2.5}$  concentration estimation model is fine-tuned by adding label data at the top layer of the model. The loss function for model fine-tuning is as follows:

$$L = \frac{1}{M} \sum_{k=1}^M (y'_i - y_i)^2, \quad (6)$$

where  $y'_i$  and  $y_i$  are the estimated and actual  $PM_{2.5}$  concentration values, respectively.  $M$  is the size of a batch. During the fine-tuning process, we compress the network model using Srinivas *et al.*'s data-free parameter pruning method [46]. In addition, after the network model training, we further compress the whole network model by employing Cai *et al.*'s weight normalization-based quantization scheme [47]. The above pruning and quantization methods are adopted because both algorithms are easy to implant and can effectively main-

tain the model's accuracy. The impact of model compression on the model's accuracy and computational speed is analyzed in Section IV C 1) and Section IV E.

#### IV. EXPERIMENTS AND DISCUSSIONS

##### A. Experimental Environment

The performance of the proposed method and other competing algorithms are tested on the benchmark AQID [23]. The AQID comprises 750 pictures with  $PM_{2.5}$  concentrations from 1 to 423  $\mu g/m^3$ . The  $PM_{2.5}$  concentration labels of the AQID were collected by professional equipment MetOne BAM-1020. At the same time, to ensure the validity of these labels, all pictures were taken within a kilometer of the device MetOne BAM-1020. The AQID contains a variety of scenes, including overpasses, squares, roads, parks, lakes, and tall buildings. We employ 80% of the AQID samples for training and the remaining 20% for testing. Referring to existing related studies, we employ Pearson linear correlation coefficient (PLCC), Spearman rank-order correlation coefficient (SROCC), and Kendall rank-order correlation coefficient (KROCC) to evaluate the performance of  $PM_{2.5}$  concentration measurement algorithms. The closer the values of PLCC, SROCC, and KROCC are to 1, the better the performance of the corresponding  $PM_{2.5}$  concentration measurement algorithm.

##### B. Performance Comparison of SOTA Methods

In this study, we collect ten competing methods to verify the effectiveness of the proposed  $PM_{2.5}$  monitoring method. The haze introduced by  $PM_{2.5}$  mainly destroys the color and structure information of images during the imaging process. Therefore, in addition to the same type of image-based  $PM_{2.5}$  monitoring algorithm, we additionally employ the popular image contrast and sharpness measurement algorithms as competing algorithms, which can be used to estimate color and structure losses of images. The image contrast measurement

algorithms include the No-reference Image Quality Metric for Contrast distortion (NIQMC) [48] and the Blind Image Quality Measure of Enhanced images (BIQME) [49]. The photo sharpness measurement algorithms consist of the Fast Image SHarpness estimator (FISH) [50], the Auto-Regressive-based Image Sharpness Metric (ARISM) [51], and the Blind Image BLur Evaluation (BIBLE) [52] algorithm. The image-based  $PM_{2.5}$  monitoring methods contain Gu *et al.*'s method [23], Yue *et al.*'s method [26], Zhang *et al.*'s method [25], Sun *et al.*'s method [27] and Wang *et al.*'s method [28]. Since the aforementioned image-based  $PM_{2.5}$  concentration measurement algorithms have been introduced in Section II, only the employed image contrast and sharpness algorithms will be briefly described here.

- **NIQMC.** NIQMC measures the quality of contrast-altered images with information measurement. Specifically, NIQME combines the significant image region's information entropy and the visual saliency mechanism to predict the degree of contrast distortion.
- **BIQME.** BIQME extracts 17-dimensional features from five aspects: image naturalness, colorfulness, brightness, sharpness and contrast. Then, these features are used for learning an enhanced image quality evaluation model, which can effectively estimate the intensity of image contrast distortion.
- **FISH.** Fish estimates the sharpness degree of an image by calculating the Log-energies of the high-frequency wavelet sub-band coefficients of the image.
- **ARISM.** Because image blurring can increase the self-similarity of local AR parameters, ARISM first measures the energy- and contrast-difference of the AR model coefficients at each pixel and further calculates image sharpness using percentile pooling.
- **BIBLE.** BIBLE uses the characteristics of discrete orthogonal moments to effectively describe the deformation of image edges to estimate image sharpness.

Table I shows the performance of the proposed vision-based monitoring method of  $PM_{2.5}$  concentration and ten competing algorithms on AQID. The proposed method achieves the PLCC, SROCC, and KROCC values of 0.889, 0.854, and 0.663, respectively, outperforming all employed competing algorithms in AQID. The BIQME, which performs relatively well in the image contrast measurement algorithms, obtains the PLCC, SROCC, and KROCC values of 0.544, 0.538, and 0.372, respectively. The performance of BIQME is far inferior to the third type of image-based  $PM_{2.5}$  concentration measurement algorithms. Compared with BIQME, the proposed method exceeded 63.4%, 58.7%, and 78.2% on the performance indicators PLCC, SROCC, and KROCC, respectively. The best-performing image sharpness measurement algorithm, FISH, achieves PLCC, SROCC, and KROCC values of 0.469, 0.411, and 0.278 on AQID. The performance of FISH is inferior to BIQME, which also shows that  $PM_{2.5}$  causes more loss to the image color during imaging than the image structure information. According to the above analysis, it isn't easy to efficiently estimate the  $PM_{2.5}$  concentration via the image

TABLE I: Performance comparison of the proposed method with three types of SOTA algorithms. Types I, II, and III represent the photo contrast measurement algorithm, the photo sharpness measurement algorithm, and the photo-based  $PM_{2.5}$  concentration measurement algorithm, respectively.

Metrics	Type	PLCC	SROCC	KROCC	Average
NIQMC [48]	I	0.423	0.443	0.297	0.388
BIQME [49]	I	0.544	0.538	0.372	0.485
FISH [50]	II	0.469	0.411	0.278	0.386
ARISM [51]	II	0.299	0.219	0.147	0.222
BIBLE [52]	II	0.125	0.080	0.054	0.086
Gu [23]	III	0.812	0.819	0.608	0.746
Yue [26]	III	—	0.782*	0.581*	—
Zhang [25]	III	0.801*	—	0.610*	—
Sun [27]	III	0.808	0.818	0.612	0.746
Wang [28]	III	0.850	0.821	0.620	0.764
Our Method	III	<b>0.889</b>	<b>0.854</b>	<b>0.663</b>	<b>0.802</b>

\*: Experimental results are from the original articles.

—: Since the original papers' source codes are not open source, these experimental results are not available.

contrast or sharpness information.

Since Yue *et al.* method mainly focuses on image saturation domain information and pays insufficient attention to structure domain information, Yue *et al.*'s method performs weaker than other picture-based  $PM_{2.5}$  concentration measurement algorithms. The Gu *et al.*'s and Zhang *et al.*'s methods measure  $PM_{2.5}$  concentrations via computing the energy entropy in image saturation and structure transformation domains, and their performance is also very similar. Although the Gu *et al.*'s and Zhang *et al.*'s methods have estimated  $PM_{2.5}$  concentration from multiple domains such as color and structure, and their performance is far less than Wang *et al.*'s algorithm and the proposed method, especially on the performance index PLCC. The reason is that these algorithms do not consider how to eliminate the influence of the image content diversity on the  $PM_{2.5}$  concentration measurement results. For example, the smooth area of an image accounts for a large proportion, and the information entropy value is less, which leads to the misjudged as excessive  $PM_{2.5}$  concentration. Wang *et al.*'s algorithm uses the dehaze image of a  $PM_{2.5}$  image as the reference information to eliminate the influence of image content diversity on the entropy-based  $PM_{2.5}$  concentration monitoring model. However, its performance is still some distance compared to our proposed algorithm. The proposed method surpasses Wang *et al.*'s algorithm by 4.6%, 4.0%, and 6.9% on the performance indexes, PLCC, SROCC, and KROCC, respectively. The reasons why the proposed method is better than Wang *et al.*'s algorithm can include two points: (a) the feature extraction based on natural scene statistics is more robust than using the dehaze image for image content normalization; and (b) the machine learner LW-DBN-DNN used in this work is more suitable for training the  $PM_{2.5}$



TABLE II: Performance comparison of the models trained by different machine learners. Priors 1 and 2 are the developed NSSA-based visual priors for the saturation and structure losses, respectively.

Machine Learner	PLCC	SROCC	KROCC	Average
SVR	0.852	0.814	0.612	0.759
RF	0.869	0.803	0.586	0.753
BLS	0.827	0.842	0.632	0.767
MLP	0.837	0.837	0.622	0.765
DNN	0.870	0.845	0.637	0.784
DBN-DNN	<b>0.898</b>	<b>0.864</b>	<b>0.671</b>	<b>0.811</b>
LW-DBN-DNN	<i>0.889</i>	<i>0.854</i>	<i>0.663</i>	<i>0.802</i>
LW-DBN-DNN (Prior 1)	0.852	0.815	0.605	0.757
LW-DBN-DNN (Prior 2)	0.851	0.818	0.607	0.759

monitoring model than the learner SVR employed in Wang *et al.*'s algorithm.

### C. Ablation Studies

1) *Validity Analysis of LW-DBN-DNN and Visual Prior Features:* To understand the contributions of our developed NSSA-based visual prior features and LW-DBN-DNN, we adopt different types of machine learning algorithms, including Support Vector Regression (SVR), Random Forest (RF), Broad Learning System (BLS), Multi-Layer Perceptron (MLP), Deep Neural Network (DNN), and DBN-DNN, to obtain multiple PM<sub>2.5</sub> concentration estimation models by combining the designed two sets of visual prior features. The SVR, RF, and DNN have been used in related works [27], [28], [41], [53] to build PM<sub>2.5</sub> concentration monitoring models.

Table II presents the comparisons of PLCC, SROCC, and KROCC between the estimated PM<sub>2.5</sub> concentrations measured by multiple PM<sub>2.5</sub> concentration monitors and the actual PM<sub>2.5</sub> concentrations. The SVR- and RF-based PM<sub>2.5</sub> concentration measurement models show the worst performance considering the three evaluation indexes. As described in Section III C, the machine learning algorithms with shallow structures are challenging to construct efficient PM<sub>2.5</sub> concentration estimation models. The DNN-based PM<sub>2.5</sub> concentration monitoring mode performs better than the BLS- and MLP-based PM<sub>2.5</sub> concentration monitoring models. The above experimental results represent that the back-propagation-based DNN is more beneficial to construct the PM<sub>2.5</sub> concentration monitoring model. Moreover, in this work, we consider that DNN is prone to falling into local optima under limited training data size due to the random initialization of weight parameters. Thus, we construct a DBN-DNN-based PM<sub>2.5</sub> concentration monitoring model, which initializes network parameters through unsupervised greedy learning and completes the PM<sub>2.5</sub> concentration measurement model training with supervised fine-tuning. The DBN-DNN-based PM<sub>2.5</sub> monitoring model achieves PLCC, SROCC, and

KROCC values of 0.898, 0.864 and 0.671, respectively. In terms of indicators PLCC, SROCC, and KROCC, the DBN-DNN-based PM<sub>2.5</sub> monitor has improved by 3.2%, 2.2%, and 5.3%, respectively, compared with the DNN-based PM<sub>2.5</sub> monitor, which indicates that initializing network parameters through unsupervised greedy learning can effectively improve the performance of the DNN-based PM<sub>2.5</sub> concentration estimation model. In order to facilitate the deployment of our PM<sub>2.5</sub> monitoring algorithm on edge devices, we carried out pruning and quantization processing on the DBN-DNN network to build a lightweight PM<sub>2.5</sub> concentration monitoring model. It can be easily seen from Table II that the performance of our proposed PM<sub>2.5</sub> monitoring model based on LW-DBN-DNN is slightly lower than that based on DBN-DNN, but its performance is still better than other regression algorithms. In section IV E, we further validated the improvement in computational speed of the proposed LW-DBN-DNN-based PM<sub>2.5</sub> monitoring model compared to the DBN-DNN-based PM<sub>2.5</sub> monitoring algorithm.

As shown in Table I, the DNN-based PM<sub>2.5</sub> concentration estimator proposed by Sun *et al.* obtained PLCC, SROCC, and KROCC values of 0.808, 0.818, and 0.612, respectively. As depicted in Table II, the PM<sub>2.5</sub> monitoring model based on the designed visual prior features and DNN achieves PLCC, SROCC, and KROCC values of 0.870, 0.845, and 0.637, respectively. Both of the above methods are based on DNN to establish PM<sub>2.5</sub> concentration measurement models. Compared with Sun *et al.*'s method, our algorithm improves by 7.6%, 3.3%, and 4.1% on PLCC, SROCC, and KROCC, respectively. This strongly indicates that our designed visual prior features based on natural scene statistical analysis are more favorable to measure PM<sub>2.5</sub> concentrations. Fig. 2 and 3 also show that the proposed visual prior features based on natural scene statistics can effectively distinguish PM<sub>2.5</sub> images with different concentration levels. In addition, to fully demonstrate the effectiveness of the proposed NSSA-based priors, we further compare the performance of the proposed priors-based PM<sub>2.5</sub> monitoring model with the PM<sub>2.5</sub> monitoring model based on the features obtained from the raw data through the DBN-DNN's AutoEncoder. The performance comparison results are shown in Fig. 5. The proposed priors-based PM<sub>2.5</sub> monitoring model achieves the PLCC, SROCC, and KROCC values of 0.889, 0.854, and 0.663, respectively, which far exceeds that of the PM<sub>2.5</sub> monitoring model based on the features obtained from the raw data through the DBN-DNN's AutoEncoder.

Moreover, we train the PM<sub>2.5</sub> concentration estimation model using each set of priors separately. Table II shows the performance comparison of PM<sub>2.5</sub> concentration monitoring models based on each proposed visual prior with all proposed visual priors. The monitoring model based on the visual prior for the saturation loss achieves PLCC, SROCC, and KROCC values of 0.852, 0.815, and 0.605 on AQID, respectively. The monitoring model based on the visual prior for the structure loss reaches PLCC, SROCC, and KROCC values of 0.851, 0.818, and 0.607 on AQID, respectively. The monitoring model based on all the designed priors achieves PLCC, SROCC, and KROCC values of 0.889, 0.854, and

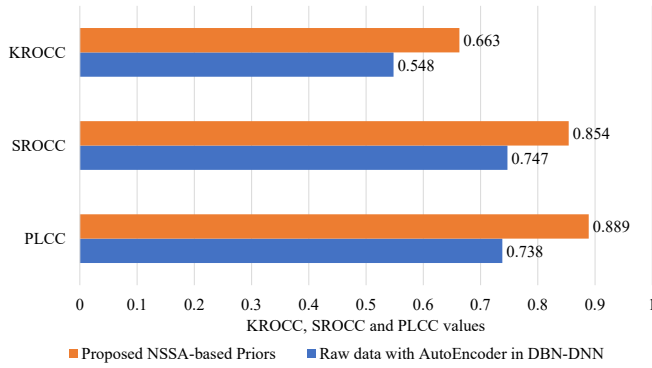


Fig. 5: Performance comparison of the proposed NSSA-based priors and the features extracted from the raw data using the DBN-DNN's AutoEncoder.

TABLE III: Performance comparison of the models with different amounts of training data.

Training-Testing	PLCC	SROCC	KROCC	Average
60%-40%	0.822	0.816	0.609	0.749
65%-35%	0.829	0.812	0.604	0.748
70%-30%	0.846	0.823	0.613	0.761
75%-25%	0.848	0.831	0.627	0.769
80%-20%	0.889	0.854	0.663	0.802
85%-15%	0.883	0.863	0.683	0.810
90%-10%	0.896	0.868	0.686	0.817
95%-05%	0.896	0.870	0.687	0.818

0.663, respectively, which shows that our proposed two types of NSSA-based visual priors are complementary to monitor  $PM_{2.5}$  concentrations.

2) *Effect of Training Data Quantity on Model Robustness:* Besides the ratio of 80%-20% of the training and testing, this part further compares the other eight training-to-test ratios, including 60%-40%, 65%-35%, 70%-30%, 75%-25%, 80%-20%, 85%-15%, 90%-10%, and 95%-05%, which are employed to validate the influence of training data size on the robustness of our  $PM_{2.5}$  measurement model. Table III shows the performance of  $PM_{2.5}$  concentration estimation models learned from different training data amounts on AQID. The experimental results show that the amount of training data determines the robustness of our  $PM_{2.5}$  monitoring model. When the amount of training data accounts for 80% of the whole dataset, the performance of the achieved  $PM_{2.5}$  monitoring model gradually stabilizes. However, our  $PM_{2.5}$  monitoring model learned at a training-test ratio of 60%-40% also reaches the performance of the mainstream algorithms at 80%-20% of the training-test ratio, such as sun *et al.*'s method (see Table I for details). Moreover, the performance of our  $PM_{2.5}$  monitoring model by a training-test ratio of 75%-25% is close to the  $PM_{2.5}$  monitoring model obtained by such as Wang *et al.*'s method with a training-test ratio of 80%-20% (see Table I for details).

TABLE IV: Generalization performance of the proposed  $PM_{2.5}$  concentration measurement algorithm across visual scenes.

Training	Testing	PLCC	SROCC	KROCC	Average
Road					
Square	Park	0.849	0.837	0.656	0.781
Building					
Park					
Square	Road	0.831	0.832	0.645	0.769
Building					
Park					
Road	Square	0.849	0.846	0.666	0.787
Building					
Park					
Road	Building	0.861	0.855	0.656	0.791
Square					

#### D. Model Robustness Analysis

1) *Illumination Influence Analysis:* At present, high-quality pictures are readily available with the help of smartphones, dashcams, and other devices. However, how to take an image suitable for measuring  $PM_{2.5}$  concentration is of great concern. Existing relevant studies [26] have conducted preliminary studies on how to collect pictures suitable for  $PM_{2.5}$  concentration monitoring and given some recommendations, such as (a) avoid shooting the sun and (b) the sky area should take up 1/3-1/2 of the whole image. Due to the significant influence of illumination on visual tasks such as object detection, object tracking, and object segmentation, this section will concentrate on the effect of illumination on the robustness of the proposed vision-based monitor of  $PM_{2.5}$  concentration. Fig. 6 presents the estimated results of our method for some images collected under different illumination intensity environments. The experimental results in Fig. 6 show that the developed photo-based  $PM_{2.5}$  monitor is difficult to achieve accurate monitoring of  $PM_{2.5}$  concentration for the images captured in low and strong illumination environments. As mentioned above, illumination has a significant impact on visual detection technology. However, our algorithm can accurately estimate  $PM_{2.5}$  concentrations through images collected under a normal illumination environment.

2) *Model Generalization Ability Analysis:* This part verifies the generalization ability of the proposed vision-based  $PM_{2.5}$  concentration monitoring algorithm across visual scenes. According to the visual content, AQID is roughly divided into four scenes: road, park, square, and building, which are the most common scenes in urban life. We employ each scene data as a testing set and three other scene data as a training set. Then, four  $PM_{2.5}$  concentration monitoring models are learned on the divided multiple training-testing sets to test the generalization ability of the proposed  $PM_{2.5}$  concentration measurement algorithm. Table IV shows the generalization



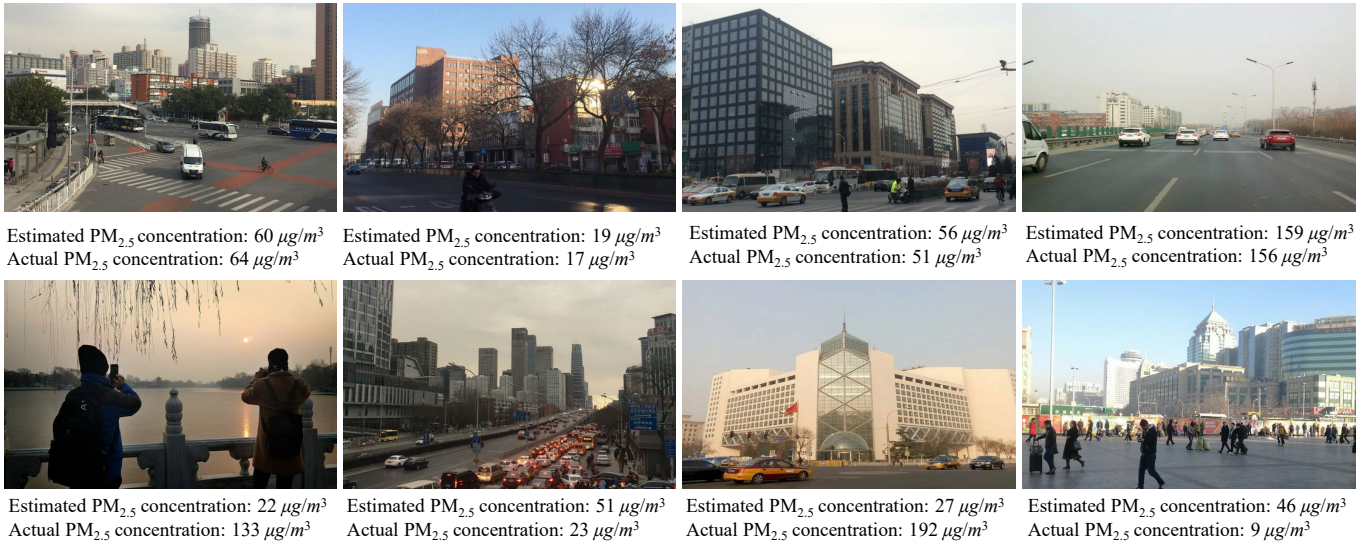


Fig. 6: Some examples of images collected under normal, low, and strong illumination environments, with actual PM<sub>2.5</sub> concentration values and PM<sub>2.5</sub> concentration values estimated by the proposed method. The first row is the images acquired in a normal illumination environment. The second row is the images obtained in low and strong illumination environments.

performance of the proposed PM<sub>2.5</sub> concentration monitoring method across visual scenes. The best PLCC, SROCC, and KROCC values obtained by our proposed method in cross-visual scene testing are 0.861, 0.855, and 0.656, respectively. The worst PLCC, SROCC, and KROCC values obtained by our proposed method in cross-visual scene testing are 0.831, 0.832, and 0.645, respectively. Compared to the performance of the proposed method on the entire benchmark in Table I, the performance of the proposed method has decreased in cross-visual scene testing. However, as shown in Table I, even the worst performance of the proposed algorithm in cross-visual scene testing still exceeds the performance of SOTA competing algorithms on the entire benchmark. In addition, the experimental results in Table IV show that the proposed method is more accurate in predicting the PM<sub>2.5</sub> concentration of building scene images.

#### E. Algorithm Running Speed

In addition to model accuracy, a model with a higher computational rate is more favored in practice. This part compares the running speed of the proposed method and Gu *et al.*'s algorithm [23], which has obvious advantages in computational efficiency [23], [26]. The source code corresponding to the two algorithms runs on the test environment (MATLAB R2022a on an Intel (R) Core (TM) i5-9400F CPU and one NVIDIA GTX 1660Ti GPU). Table V presents the experimental results of the algorithm running speed. The times recorded in Table V are the mean running time of AQID containing 750 images with resolutions of 500×261 to 978×550. According to the experimental results, the proposed PM<sub>2.5</sub> concentration measurement algorithm based on natural scene statistics improves the running rate and accuracy compared with the existing SOTA methods. In addition, the developed LW-DBN-DNN-based PM<sub>2.5</sub> monitoring model further improves the computational efficiency.

TABLE V: Comparison of the running speed between the proposed method and the PPC algorithm.

Method	Gu	Pro. (DBN-DNN)	Pro. (LW-DBN-DNN)
Time (s)	0.026	0.024	0.019

#### V. CONCLUSION

In this paper, we have developed a new vision-based PM<sub>2.5</sub> concentration measurement algorithm. Inspired by the saturation and dark channel information that can reflect the PM<sub>2.5</sub> concentration, two natural scene statistical analysis-based visual priors are specifically developed in the saturation and dark channel domains, which can effectively represent the image color and structure losses. After the visual prior extraction, we develop a lightweight deep belief network and deep neural network to train our PM<sub>2.5</sub> concentration measurement model. Experimental results show that the proposed PM<sub>2.5</sub> concentration measurement method has improved the efficiency and accuracy compared with popular state-of-the-art photo-based PM<sub>2.5</sub> concentration estimation algorithms, especially PM<sub>2.5</sub> estimation accuracy has been greatly enhanced. However, the robustness of visible visual information-based PM<sub>2.5</sub> concentration measurement algorithms is vulnerable to the illumination environment. In the future, we consider fusing multi-sensor data (e.g., infrared and hyperspectral data) to enable more robust vision-based measurement of PM<sub>2.5</sub> concentration.

#### REFERENCES

- [1] M. A. Fekih, W. Bechkit, H. Rivano, M. Dahan, F. Renard, L. Alonso, and F. Pineau, "Participatory air quality and urban heat islands monitoring system," *IEEE Transactions on Instrumentation and Measurement*, vol. 70, pp. 1–14, 2021.

- [2] Z. Chen, T. Zhang, Z. Chen, Y. Xiang, Q. Xuan, and R. P. Dick, "Hvaq: A high-resolution vision-based air quality dataset," *IEEE Transactions on Instrumentation and Measurement*, vol. 70, pp. 1–10, 2021.
- [3] K. Gu, J. Qiao, and W. Lin, "Recurrent air quality predictor based on meteorology- and pollution-related factors," *IEEE Transactions on Industrial Informatics*, vol. 14, no. 9, pp. 3946–3955, 2018.
- [4] J. Yang, Z. Zeng, K. Wang, H. Zou, and L. Xie, "Garbagenet: A unified learning framework for robust garbage classification," *IEEE Transactions on Artificial Intelligence*, vol. 2, no. 4, pp. 372–380, 2021.
- [5] Y. Li, Q. Liao, X. Zhao, Y. Tao, Y. Bai, and L. Peng, "Premature mortality attributable to pm2.5 pollution in china during 20082016: Underlying causes and responses to emission reductions," *Chemosphere*, vol. 263, p. 127925, 2021.
- [6] Y. Guo, S. Tong, Y. Zhang, A. G. Barnett, Y. Jia, and X. Pan, "The relationship between particulate air pollution and emergency hospital visits for hypertension in Beijing, China," *Science of the Total Environment*, vol. 408, no. 20, pp. 4446–4450, 2010.
- [7] G. Wang, R. Jiang, Z. Zhao, and W. Song, "Effects of ozone and fine particulate matter (PM2.5) on rat system inflammation and cardiac function," *Toxicology Letters*, vol. 217, no. 1, pp. 23–33, 2013.
- [8] A. P. Davel, M. Lemos, L. M. Pastro, S. C. Pedro, P. A. de Andre, C. Hebeda, S. H. Farsky, P. H. Saldiva, and L. V. Rossoni, "Endothelial dysfunction in the pulmonary artery induced by concentrated fine particulate matter exposure is associated with local but not systemic inflammation," *Toxicology*, vol. 295, no. 1–3, pp. 39–46, 2012.
- [9] R. D. Brook, S. Rajagopalan, C. A. Pope III, J. R. Brook, A. Bhatnagar, A. V. Diez-Roux, F. Holguin, Y. Hong, R. V. Luepker, M. A. Mittleman *et al.*, "Particulate matter air pollution and cardiovascular disease: an update to the scientific statement from the american heart association," *Circulation*, vol. 121, no. 21, pp. 2331–2378, 2010.
- [10] K.-H. Kim, S. A. Jahan, E. Kabir, and R. J. Brown, "A review of airborne polycyclic aromatic hydrocarbons (pahs) and their human health effects," *Environment International*, vol. 60, pp. 71–80, 2013.
- [11] V. Aboyans, C. of Death Collaborators *et al.*, "Global, regional, and national age-sex specific all-cause and cause-specific mortality for 240 causes of death, 1990–2013: a systematic analysis for the global burden of disease study 2013," *The Lancet (British edition)*, vol. 385, no. 9963, pp. 117–171, 2015.
- [12] Q. Zhang, J. Quan, X. Tie, X. Li, Q. Liu, Y. Gao, and D. Zhao, "Effects of meteorology and secondary particle formation on visibility during heavy haze events in Beijing, China," *Science of the Total Environment*, vol. 502, pp. 578–584, 2015.
- [13] Y. Liu, Z. Ning, Y. Chen, M. Guo, Y. Liu, N. K. Gali, L. Sun, Y. Duan, J. Cai, D. Westerdahl, X. Liu, K. Xu, K.-f. Ho, H. Kan, Q. Fu, and K. Lan, "Aerodynamic analysis of SARS-CoV-2 in two Wuhan hospitals," *Nature*, vol. 582, no. 7813, pp. 557+, 2020.
- [14] H. Daraei, K. Toolabian, M. Kazempour, and M. Javanbakht, "The role of the environment and its pollution in the prevalence of COVID-19," *Journal of Infection*, vol. 81, no. 2, pp. E168–E169, 2020.
- [15] M. Rohrer, A. Flahault, and M. Stoffel, "Peaks of fine particulate matter may modulate the spreading and virulence of COVID-19," *Earth Systems and Environment*, vol. 4, no. 4, pp. 789–796, 2020.
- [16] G. Myhre, B. H. Samset, M. Schulz *et al.*, "Radiative forcing of the direct aerosol effect from AeroCom Phase II simulations," *Atmospheric Chemistry and Physics*, vol. 13, no. 4, pp. 1853–1877, 2013.
- [17] H. Zhang, S. Zhao, Z. Wang, X. Zhang, and L. Song, "The updated effective radiative forcing of major anthropogenic aerosols and their effects on global climate at present and in the future," *International Journal of Climatology*, vol. 36, no. 12, pp. 4029–4044, 2016.
- [18] M. A. Bollasina, Y. Ming, and V. Ramaswamy, "Anthropogenic aerosols and the weakening of the south asian summer monsoon," *Science*, vol. 334, no. 6055, pp. 502–505, 2011.
- [19] B. Smeets, S. Pfenninger, S. Yang, D. Folini, B. van der Zwaan, and M. Wild, "Estimation of losses in solar energy production from air pollution in China since 1960 using surface radiation data," *Nature Energy*, vol. 4, no. 8, pp. 657–663, 2019.
- [20] J. Chow, "Measurement methods to determine compliance with ambient air-quality standards for suspended particles," *Journal of the Air & Waste Management Association*, vol. 45, no. 5, pp. 320–382, 1995.
- [21] Y. Peng, Z. Sui, Y. Zhang, T. Wang, P. Norris, and W.-P. Pan, "The effect of moisture on particulate matter measurements in an ultra-low emission power plant," *Fuel*, vol. 238, pp. 430–439, 2019.
- [22] K. He, J. Sun, and X. Tang, "Single image haze removal using dark channel prior," *IEEE Transactions on Pattern Analysis and Machine Intelligence*, vol. 33, no. 12, pp. 2341–2353, 2011.
- [23] K. Gu, J. Qiao, and X. Li, "Highly efficient picture-based prediction of pm2.5 concentration," *IEEE Transactions on Industrial Electronics*, vol. 66, no. 4, pp. 3176–3184, 2019.
- [24] X. Wang, M. Wang, X. Liu, X. Zhang, and R. Li, "A pm2.5 concentration estimation method based on multi-feature combination of image patches," *Environmental Research*, vol. 211, p. 113051, 2022.
- [25] H. Zhang, D. Peng, W. Chen, and X. Xu, "Extremely efficient PM2.5 estimator based on analysis of saliency and statistics," *Electronics Letters*, vol. 55, no. 1, pp. 30–31, 2019.
- [26] G. Yue, K. Gu, and J. Qiao, "Effective and efficient photo-based pm2.5 concentration estimation," *IEEE Transactions on Instrumentation and Measurement*, vol. 68, no. 10, pp. 3962–3971, 2019.
- [27] K. Sun, L. Tang, J. Qian, G. Wang, and C. Lou, "A deep learning-based pm2.5 concentration estimator," *Displays*, vol. 69, p. 102072, 2021.
- [28] G. Wang, Q. Shi, H. Wang, K. Sun, Y. Lu, and K. Di, "Multi-modal image feature fusion-based pm2.5 concentration estimation," *Atmospheric Pollution Research*, vol. 13, no. 3, p. 101345, 2022.
- [29] K. Abutalip, A. Al-Lahham, and A. El Saddik, "Digital twin of atmospheric environment: Sensory data fusion for high-resolution pm2.5 estimation and action policies recommendation," *IEEE Access*, vol. 11, pp. 14 448–14 457, 2023.
- [30] P. Castello, C. Muscas, P. A. Pegoraro, and S. Sulis, "Improved fine particles monitoring in smart cities by means of advanced data concentrator," *IEEE Transactions on Instrumentation and Measurement*, vol. 70, pp. 1–9, 2021.
- [31] M. Ferro, V. Paciello, A. Pietrosanto, and P. Sommella, "A distributed measurement system for the estimation of air quality," *IEEE Instrumentation & Measurement Magazine*, vol. 23, no. 5, pp. 51–56, 2020.
- [32] M. Yao, D. Tao, J. Wang, R. Gao, and K. Sun, "Marvair: Meteorology augmented residual-based visual approach for crowdsourcing air quality inference," *IEEE Transactions on Instrumentation and Measurement*, vol. 71, pp. 1–10, 2022.
- [33] M. Nakata, T. Moriyama, I. Sano, and S. Mukai, "Analysis of factors affecting pm2.5 concentration in the mountainous areas of japan through ground observations and simulations," in *2021 IEEE International Geoscience and Remote Sensing Symposium IGARSS*, 2021, pp. 7248–7251.
- [34] Y. Wang, Y. Yuan, Q. Wang, C. Liu, Q. Zhi, and J. Cao, "Changes in air quality related to the control of coronavirus in china: Implications for traffic and industrial emissions," *Science of The Total Environment*, vol. 731, Aug 20 2020.
- [35] K. Gu, H. Liu, J. Liu, X. Yu, T. Shi, and J. Qiao, "Air pollution prediction in mass rallies with a new temporally-weighted sample-based multitask learner," *IEEE Transactions on Instrumentation and Measurement*, vol. 71, pp. 1–15, 2022.
- [36] A. Mittal, A. K. Moorthy, and A. C. Bovik, "No-reference image quality assessment in the spatial domain," *IEEE Transactions on Image Processing*, vol. 21, no. 12, pp. 4695–4708, 2012.
- [37] A. Mittal, R. Soundararajan, and A. C. Bovik, "Making a completely blind image quality analyzer," *IEEE Signal Processing Letters*, vol. 20, no. 3, pp. 209–212, 2013.
- [38] S. V. Reddy Dendi and S. S. Channappayya, "No-reference video quality assessment using natural spatiotemporal scene statistics," *IEEE Transactions on Image Processing*, vol. 29, pp. 5612–5624, 2020.
- [39] K. He, J. Sun, and X. Tang, "Single image haze removal using dark channel prior," in *2009 IEEE Conference on Computer Vision and Pattern Recognition*, 2009, pp. 1956–1963.
- [40] N. Otsu, "A threshold selection method from gray-level histograms," *IEEE Transactions on Systems, Man, and Cybernetics*, vol. 9, no. 1, pp. 62–66, 1979.
- [41] Z. Xia, "A robust photo-based PM2.5 monitoring method by combining linear and non-linear learning," *IET Image Processing*, 2022.
- [42] Z. Zhang, G. Chen, and S. Chen, "A support vector neural network for p300 eeg signal classification," *IEEE Transactions on Artificial Intelligence*, vol. 3, no. 2, pp. 309–321, 2022.
- [43] G. E. Hinton, S. Osindero, and Y.-W. Teh, "A fast learning algorithm for deep belief nets," *Neural Computation*, vol. 18, no. 7, pp. 1527–1554, 2006.
- [44] G. E. Hinton and R. R. Salakhutdinov, "Reducing the dimensionality of data with neural networks," *Science*, vol. 313, no. 5786, pp. 504–507, 2006.
- [45] G. E. Hinton, "Deep belief networks," *Scholarpedia*, vol. 4, no. 5, p. 5947, 2009.
- [46] S. Srinivas and R. V. Babu, "Data-free parameter pruning for deep neural networks," in *British Machine Vision Conference*, 2015, pp. 31.1–31.12.
- [47] W.-P. Cai and W.-J. Li, "Weight normalization based quantization for deep neural network compression," 2019.

- [48] K. Gu, W. Lin, G. Zhai, X. Yang, W. Zhang, and C. W. Chen, "No-reference quality metric of contrast-distorted images based on information maximization," *IEEE Transactions on Cybernetics*, vol. 47, no. 12, pp. 4559–4565, 2017.
- [49] K. Gu, D. Tao, J.-F. Qiao, and W. Lin, "Learning a no-reference quality assessment model of enhanced images with big data," *IEEE Transactions on Neural Networks and Learning Systems*, vol. 29, no. 4, pp. 1301–1313, 2018.
- [50] P. V. Vu and D. M. Chandler, "A fast wavelet-based algorithm for global and local image sharpness estimation," *IEEE Signal Processing Letters*, vol. 19, no. 7, pp. 423–426, 2012.
- [51] K. Gu, G. Zhai, W. Lin, X. Yang, and W. Zhang, "No-reference image sharpness assessment in autoregressive parameter space," *IEEE Transactions on Image Processing*, vol. 24, no. 10, pp. 3218–3231, 2015.
- [52] L. Li, W. Lin, X. Wang, G. Yang, K. Bahrami, and A. C. Kot, "No-reference image blur assessment based on discrete orthogonal moments," *IEEE Transactions on Cybernetics*, vol. 46, no. 1, pp. 39–50, 2016.
- [53] K. Sun, L. Tang, S. Huang, and J. Qian, "A photo-based quality assessment model for the estimation of pm2.5 concentrations," *IET Image Processing*, vol. 16, no. 4, pp. 1008–1016, 2022.



**Guangcheng Wang** received the B.S. degree from Changzhou Institute of Technology, Changzhou, China, in 2015, the M.S. degree from China University of Mining and Technology, Xuzhou, China, in 2018, and the Ph.D. degree from Wuhan University, Wuhan, China, in 2022. He is currently an associate professor with the Nantong University, Nantong, China. His research interests include image processing, multimedia quality assessment and environmental perception.



**Quan Shi** received the M.S. and Ph.D. degrees in management information systems from the University of Shanghai for Science and Technology, Shanghai, China, in 2005 and 2011, respectively. He is currently a Professor with the School of Transportation, Nantong University, Nantong, China. His research interests include the development of signal and image processing and big data techniques.



**Han Wang** received a B.S. degree from Shenyang Ligong University, in 2003, M.S. degree from Northeastern University, in 2007 and Ph.D. degree in Electrical Engineering from Korea University, in 2015.

In 2016, he joined the faculty of school of Transportation at Nantong University. Since 2019, he has been an Associate Professor with the School of Transportation and Civil Engineering. His current research interests are multimodal image processing, computer vision and deep learning.



**Ke Gu** (Senior Member, IEEE) received the B.S. and Ph.D. degrees from Shanghai Jiao Tong University Shanghai, China, in 2009 and 2015. He is currently a Professor with Beijing University of Technology, Beijing, China. His research interests include industrial vision, environmental perception, image processing and machine learning.



**Mengting Wei** received the B.S. degree from Beijing Foreign Studies University, Beijing, China, in 2010, and the master's degree from University of Hertfordshire, Hatfield, United Kingdom, in 2015. Her interests include artificial intelligence and machine learning.



**Lai Kuan Wong** received the B.Sc. degree in computer science from Universiti Sains Malaysia, George Town, Malaysia and the M.Sc. and Ph.D. degrees in computing from the National University of Singapore, Singapore. She is a Senior Lecturer with Faculty of Computing and Informatics, Multimedia University, Cyberjaya, Malaysia. Her research interests include computational photography, stereo image and video enhancement, and 3D data visualization and medical imaging.



**Mingxing Wang** received the B.S. degree from China University of Mining and Technology-Beijing, Beijing, China, in 2007, and the master's degree from Kunming University of Science and Technology, Kunming, China, in 2015. She is currently the general manager of Century Rotek (Beijing) Environmental Science and Technology Co., Ltd. Her interests include artificial intelligence and machine learning.